International Journal of Plasticity 149 (2022) 103152

Contents lists available at ScienceDirect

International Journal of Plasticity

journal homepage: www.elsevier.com/locate/ijplas

Modeling the competition between solid solution and precipitate strengthening of alloys in a 3D space

Qihong Fang [a], Zhen Huang [a], Li Li [a], Zaiwang Huang [b], Bin Liu [b], Yong Liu [b], Jia Li [a,*], Peter K. Liaw [c]

[a] State Key Laboratory of Advanced Design and Manufacturing for Vehicle Body, College of Mechanical and Vehicle Engineering, Hunan University, Changsha 410082, PR China

[b] State Key Laboratory of Powder Metallurgy, Central South University, Changsha 410083, PR China

[c] Department of Materials Science and Engineering, The University of Tennessee, Knoxville, TN 37996, USA

ARTICLE INFO

Keywords:
3D space
Precipitate
Cooling rate
Alloy
Yielding strength

ABSTRACT

Until now, the nature of the competitive and cooperative correlation between solid solution strengthening and precipitate hardening is still uncovered, and then brings great challenges in designing the high-performance alloys. Here, a unified model has been developed to establish the quantitative relationships among the aging process, microstructure, and yielding strength for a model nickel-based superalloy in a three-dimensional (3D) space, which agglomerates the three independent variables of aging temperature, cooling time, and matrix composition, and these variables dominated the size and volume fraction of precipitates, and anti-phase boundary (APB) energy. Our experiments clearly suggest the competitive and cooperative correlation of solid solution and precipitate hardening exits in a 3D space. The size and volume fraction of precipitates, and the composition of matrix after the aging process can be predicted, and then integrated into the physical model to obtain the yielding strength of alloys. On average, the deviation of the yielding strength is 4%, which is far better than 15% with the existing strength model without considering the heat treatment, significantly reducing the development cycle. The size and volume fraction of precipitates decrease with the increased cooling rate, leading to that the precipitate strengthening firstly increases and then decreases. Meanwhile, this trend would result in enhancing solid solution strengthening monotonously. Especially, the critical cooling rate coordinates the relationship between the competition and cooperation owing to the obvious change of the APB energy together with the matrix composition, and a maximum yielding strength occurs at 166 ℃/min. The present work can provide a key theoretical guidance for designing advanced alloys with the excellent performance in a 3D space.

1. Introduction

The nickel-based superalloys are extensively utilized in the hot-end components due to their excellent properties at high temperatures (Pollock, 2016; Xu et al., 2017; Murray et al., 2020; Panwisawas et al., 2020; Wu et al., 2020; Wei et al., 2021). The extraordinary high-temperature performance is essentially originating from the special contribution of solid solution strengthening

---

[*] Corresponding author.
E-mail address: lijia123@hnu.edu.cn (J. Li).

https://doi.org/10.1016/j.ijplas.2021.103152
Received 27 August 2021; Received in revised form 8 November 2021;
Available online 17 November 2021

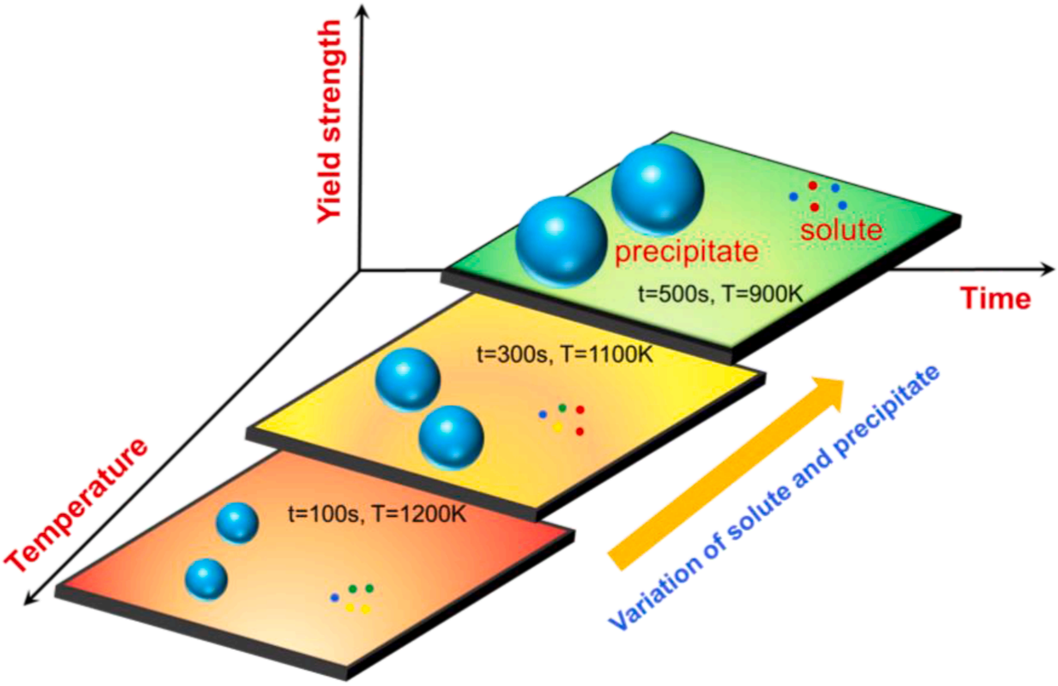

Fig. 1. The mechanical properties of alloys in a 3D space, which contains three independent variables of the aging temperature, cooling time, and matrix composition. These three independent variables would control the size and volume fraction of the precipitate, and APB energy.

and precipitate strengthening, which is mainly controlled by the unique microstructures of precipitates (Reed, 2008; Osada et al., 2013; Francis et al., 2014; Li et al., 2015; Ji et al., 2019; Schleifer et al., 2020). The microstructural parameters of precipitates are dependent on the special heat treatment conditions, which are composed of the solution treatment and subsequent aging treatment. It is generally recognized that the cooling rate plays a crucial role on the microstructural evolution and mechanical properties of nickel-based superalloys.

The relationships between the cooling rate and the precipitate configuration have been widely reported in the previous work (Li et al., 2018; Mallikarjuna et al., 2019; Li et al., 2021). The experiments show that the size of the nanoscale precipitates presents a monomodal distribution when the cooling rate is high. The slow cooling rate produces a bimodal distribution of the precipitates with a large size and irregular cubic shape (Li et al., 2018; Mallikarjuna et al., 2019). This reason is that the lower cooling rate promotes the element migration of the precipitates, and then the size and volume fraction of the precipitates increase at a low cooling rate (Li et al., 2021). Through the numerical simulations of precipitate kinetics, the unimodal and multimodal size distribution of the precipitates is observed in the continuous cooling process, and also verified based on the previous research (Radis et al., 2009). Using the thermodynamic calculations, the key kinetic factors are the compositional variations of precipitates for different cooling rates due to that the diffusion mechanism changes with the temperature (Chen et al., 2015). Based on the classic-nucleation theory and diffusion-growth theory, a fast-acting model is developed to calculate the number density and size variation of the precipitates during the continuous cooling (Semiatin et al., 2015, 2018).

Moreover, other physical models have been developed, which try to modify the classic theories of solid solution strengthening and precipitate strengthening. For instance, a grain-size dependent solution pinning model is proposed, and predicts the solid solution softening behavior in the nanocrystal alloy (Rupert et al., 2011). Based on the Mooren’s approach, the classical solid solution strengthening model has been extended to calculate the solid solution hardening in the high entropy alloys (Toda-Caraballo and Rivera-Díaz-del-Castillo, 2015). In consideration of the composition-related lattice constant and shear modulus, the solid solution strengthening effect of various alloy elements is calculated by high throughput density functional theory (Wang et al., 2021). As for the precipitate strengthening, a parameter-free physical model that considers the size distribution of the multimodal precipitates is proposed (Galindo-Nava et al., 2015), and this model can accurately predict the yielding stress. The effect of chemical element concentration on various strengthening mechanisms is elucidated. It is found that the multifaceted effect of the element is more significant than the variation of the precipitate volume fraction (Goodfellow et al., 2019). By introducing the temperature-dependent microstructural parameters, a yielding strength model for nickel-based superalloys at different temperatures is developed (Li et al., 2019). Considering the relative position between the dislocation-slip plane and the precipitate-geometric center, a probability-dependent precipitate strengthening model is proposed (Fang et al., 2019). This model could predict the contribution of precipitate strengthening more accurately in a wide range of precipitate size. By incorporation of the additional cube slip system, the γ-γ' interaction, and the adoption of APB shearing as the dominant deformation mechanism in the γ and γ' phases, a dislocation density-based crystal plasticity model is developed to capture the micromechanical behavior of nickel-based superalloys (Gupta and

Table 1
The nominal composition of a nickel-based alloy (weight percent, wt %).

Element	Co	Cr	Mo	W	Al	Ti	Nb	C	B	Zr	Hf	Ni
Alloy	26	13	4	4	3.2	3.7	0.95	0.05	0.025	0.05	0.2	Bal.
precipitate	14.09	1.173	0.19	2.44	6.35	7.77	1.98	-	-	0.018	0.18	Bal.

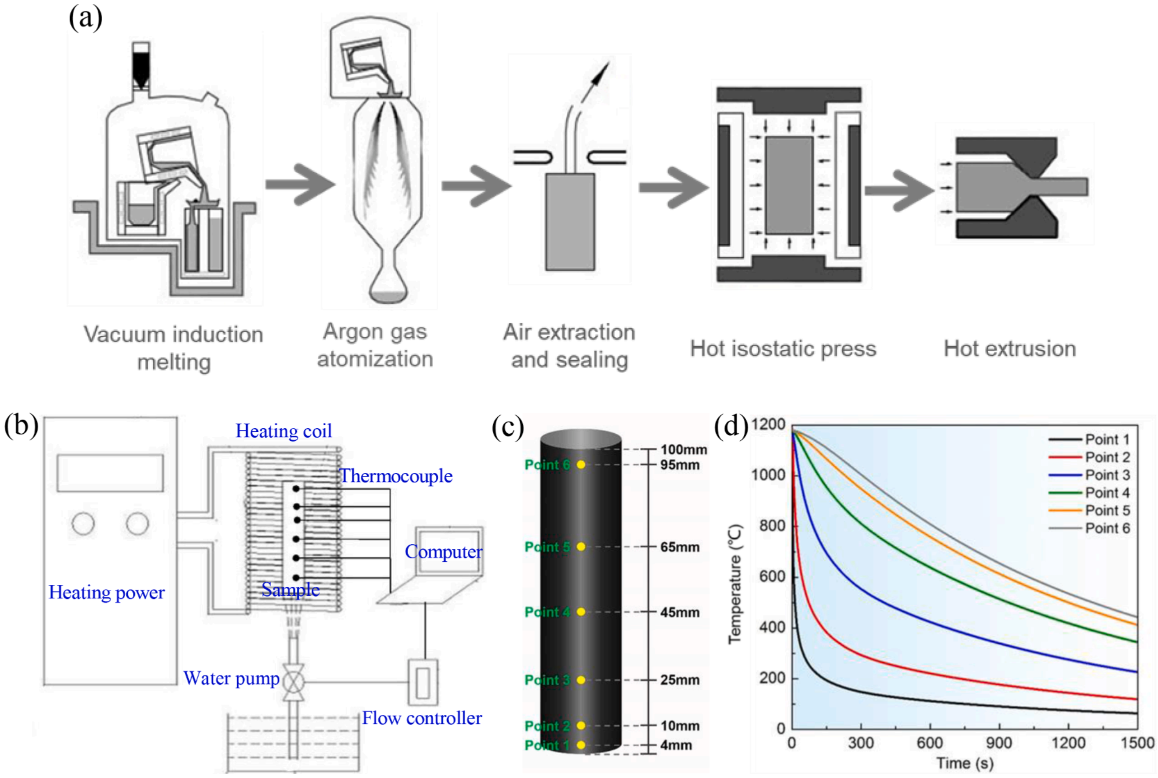

Fig. 2. (a) The schematic of the preparation of the investigated alloy. (b) The schematic diagram of equipment for end quenching, which can realize high-throughput precipitate control and data acquisition. (c) The selected 6 points on the gradiently-cooled specimen, where the thermocouples are welded on the selected point to monitor the temperature during water quenching. (d) The change of temperature for the points 1–6 with the increase of the cooling time.

Bronkhorst, 2021). Recently, a series of tie-line single-crystal modeling specimens are uniquely designed for the direct validation of classical precipitate strengthening theory. The result shows that the experimental measured strength does not correlate well with the value predicted by the classical precipitate strengthening model (Wu et al., 2021). The previous work reported above has been committed to improving the classical model of solid solution strengthening and precipitate strengthening, and then has been extended to some novel materials, such as nanocrystal alloys, high-entropy alloys, and high-temperature alloys. However, the competitive and cooperative mechanism between solid solution strengthening and precipitate strengthening to the yielding strength during the heat-treatment process is rarely reported, which is a significant and necessary issue for the design and industrial application of high-strength alloys.

As a hopeful advanced powder metallurgy (PM) technique, hot isostatic pressing (HIP) has been extensively explored to obtain attractive mechanical properties in the previous fundamental research (Atkinson and Davies, 2000; Singh et al., 2020). HIP can rapidly fabricate nearly full dense and complex components with fine microstructures and excellent mechanical properties directly from loose metal powders (Han et al., 2018; Gussev et al., 2018; Qin et al., 2021). It is well known that HIP is not only employed to eliminate the internal pores in a material, but also thought to be particularly effective as a post treatment of selective laser melting process (Hirata et al., 2020; Du Plessis and Macdonald, 2020; Herzog et al., 2020). The nickel based superalloy turbine disc used in aeroengines are usually fabricated via HIP technique (Wei et al., 2014; Sreenu et al., 2020). Here, we would employ the HIP technology to fabricate the superalloys.

In the current work, a new model for the quantitative correlation among the processing parameter, microstructure, and yielding strength is established for the alloy in a 3D space agglomerating the temperature, time, and composition. Several corresponding sub-problems should be solved: (i) The size and volume fraction of the precipitates with the increase of the cooling rate are firstly determined, based on the experimental data. (ii) Subsequently, considering the actual precipitate spatial and statistical distribution, a

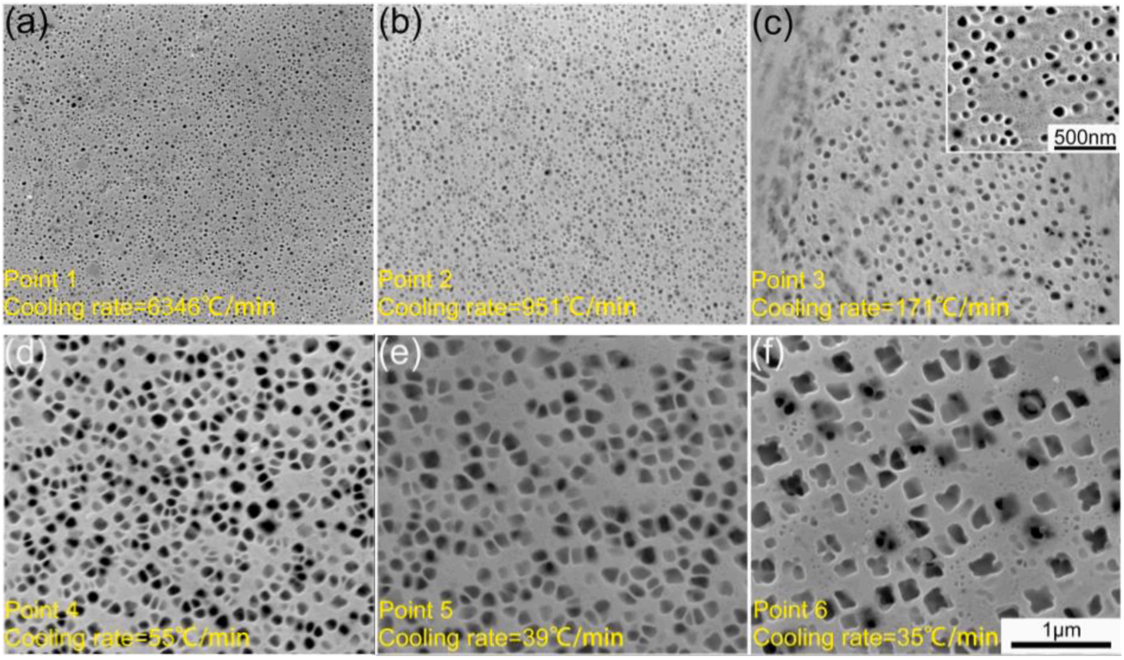

Fig. 3. The evolution of precipitates at different cooling rates after end quenching. The point 1 is cooled at 6346 °C/min (a), the point 2 at 951 °C/min (b), the point 3 at 171 °C/min (c), the point 4 at 55 °C/min (d), the point 5 at 39 °C/min (e), and the point 6 at 35 °C/min (f).

precipitate strengthening model is proposed. (iii) Meanwhile, considering the composition variation of the matrix, the solid solution strengthening is developed. (iv) By combining the precipitate strengthening and solid solution strengthening, a yielding strength model is established. (v) Finally, integrating the temperature- and time-dependent size and volume fraction of the precipitate into the strength model, a yielding strength model can be developed after the heat-treatment process. Fig. 1 illustrates the predicted mechanical properties for alloys in a 3D space. Based on this result, the competitive and cooperative mechanisms between the solid solution and precipitate strengthening would be revealed from a high-dimension aspect.

2. Experiment

2.1. Material preparation and heat treatment

A nominal chemical composition of a nickel-based superalloy in the present work is listed in Table 1. Firstly, the alloy powders are prepared, using a vacuum-induction melting technique and atomized by argon gas. A stainless-steel container is employed to contain the alloy powders with sizes ranging from 50 to 150 μm. Then, HIP is performed in a vacuum condition of 1100 °C/140 MPa, and the alloy powders are consolidated for 4 h. After the HIP treatment, we remove the stainless steel container and heat-extrude (HEX) the billet at 1100 °C to reduce the billet area to one-tenth of the original. The alloy sample with a diameter of 25 mm and a length of 100 mm from the HEX billet is used for end quenching. The detail process is presented in Fig. 2a. The top end and the side surfaces of the alloy are coated by the ceramic fibre wool to prevent heat loss, and the bottom surface is exposed for subsequent water quenching till to room temperature. The sample is a supersolvus solution treated at 1180 °C for 40 min, and then end quenched at 650 °C, where the solvus temperature of this alloy is 1154 °C. The six thermocouples are welded on the specimen side surface to monitor the temperature, where every thermocouple is set as the point, as presented in Fig. 2b. The thermocouple positions are selected in the prepared sample with the increased cooling rate (Fig. 2c).

In order to quantify the solid solution cooling rate at different positions of the gradient cooling sample, the formula,$c = (T_{sol} - T_{end})/\Delta t$, is used to determine the solid solution cooling rate in the area from points 1–6, whose method refers to the literature and the actual experience of General Aviation in the United States (Mao et al., 2001, 2002). Here, c is the solid solution cooling rate, T_{sol} is the solid solution treatment temperature of 1180 °C, T_{end} is the temperature end point, which is set to a fixed value of 650 °C, and Δt is the time required to cool from the solid solution temperature to the end temperature for a certain point in the sample. Hence, the corresponding cooling rates of six points from the sample are 35, 39, 55, 171, 951, and 6346 °C/min, based on the developed end quenching equipment (Fig. 2d), which is used for the high-throughput experimental preparation and data acquisition.

2.2. Microstructural characterization

Using a FEI Quanta 650 scanning electron microscope (SEM) equipped with an electron backscattered diffraction (EBSD) analyzer

Table 2
The average radius and volume fraction of precipitates, the average grain size and the Vickers hardness obtained from the experiment.

Point	Average precipitate radius, r (nm)	Precipitate volume fraction, f (%)	Grain size, D (μm)	Vickers hardness (Hv)
1	11.1 ± 2.6	13.9	9.65	430.96
2	13.9 ± 2.0	15.4	9.38	464.71
3	33.3 ± 8.0	20.0	10.0	494.12
4	49.5 ± 14.2	31.3	9.94	454.49
5	61.1 ± 20.9	34.6	9.53	447.68
6	80.7 ± 34.7	35.6	10.58	432.51

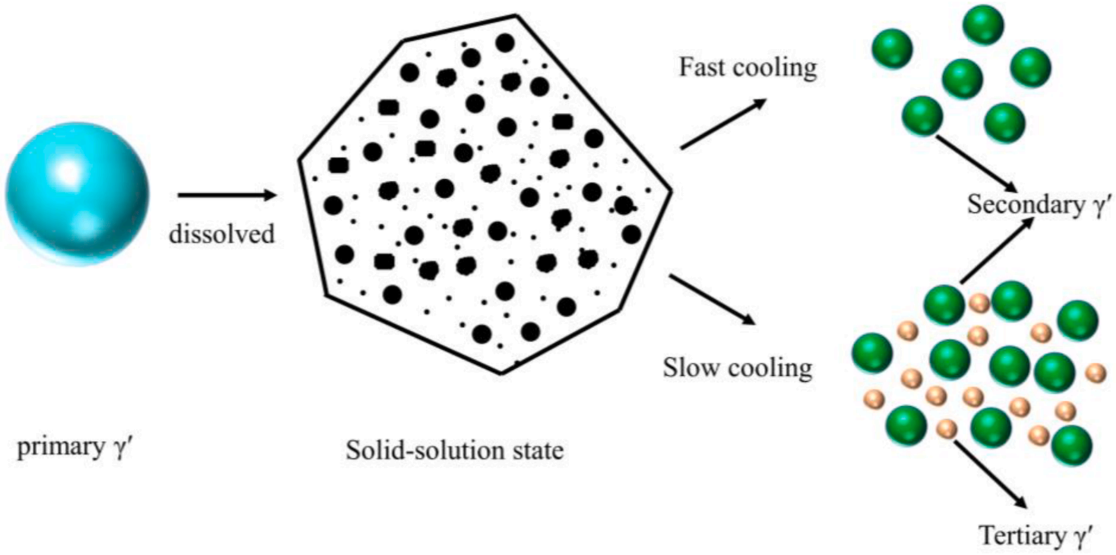

Fig. 4. The dissolution and re-precipitation mechanisms of precipitates, where the primary precipitate is transformed into secondary precipitate during the fast cooling condition, and the primary precipitate is transformed into a tertiary precipitate during the slow cooling condition.

and transmission electron microscope (TEM), the microstructure of the nickel-based superalloy is characterized. Fig. 3 shows the morphology, size, and volume fraction of precipitates at various cooling rates. The statistical results show (i) the precipitate size is unimodally distributed at the fast cooling rate; (ii) with the gradually-decreasing cooling rate, the secondary precipitates coarsen, and the tertiary precipitates gradually nucleate and grow. The precipitate size is bimodally distributed at the low cooling rate. For the case of high cooling rate, such as 6346 and 951 °C/min, the secondary precipitates are spherical due to the leading role of the isotropic interface energy (Singh et al., 2013). Through measuring the image pixel, Table 2 presents the average radius and volume fraction of the precipitate and the average grain size from the points 1–6. Here, the radius of the secondary γ' precipitate is counted for the points 1–6, and the volume fraction includes the secondary γ' precipitate and tertiary γ' precipitate. Although a bimodal precipitate size distribution exists, the volume fraction of only one type of precipitate is dominant (Masoumi et al., 2016; Smith et al., 2018). In addition, the average grain size of points 1–6 is approximately equivalent, indicating that no substantial grain growth occurs during the end quenching. According to the previous work (Osada et al., 2013), there is a quantitative relationship between the Vickers hardness and yield strength of nickel-based superalloys. Considering the size limitation of the gradient cooling sample, we employ the Vickers hardness to study the mechanical properties of the sample at different points.

3. Microstructure-based physical model in a 3D space

3.1. Model of precipitate size

The precipitate strengthening is the single most important contribution to the nickel-based superalloys, which provide not only the excellent yield strength from the interaction between the dislocation and precipitate, but also high work hardening from the short range stress field (Khan and Meredith, 2010). The microstructure parameter and morphology of precipitates in alloys are greatly affected by the cooling rate. In fact, the cooling rate is determined, based on the dependence of temperature on time. In order to obtain the precipitates with different sizes and morphologies, the alloys are heated to a solid-solution temperature, and then cooled (Fig. 4). Due to the fact that the elemental redistribution in the matrix and precipitate is significantly affected by the cooling rate, the composition and structure of precipitates during continuous cooling are controlled by the concentration gradients (Reinhart et al., 2020). Here, considering the quenching temperature and cooling time, the size and volume fraction of the precipitate can be modeled.

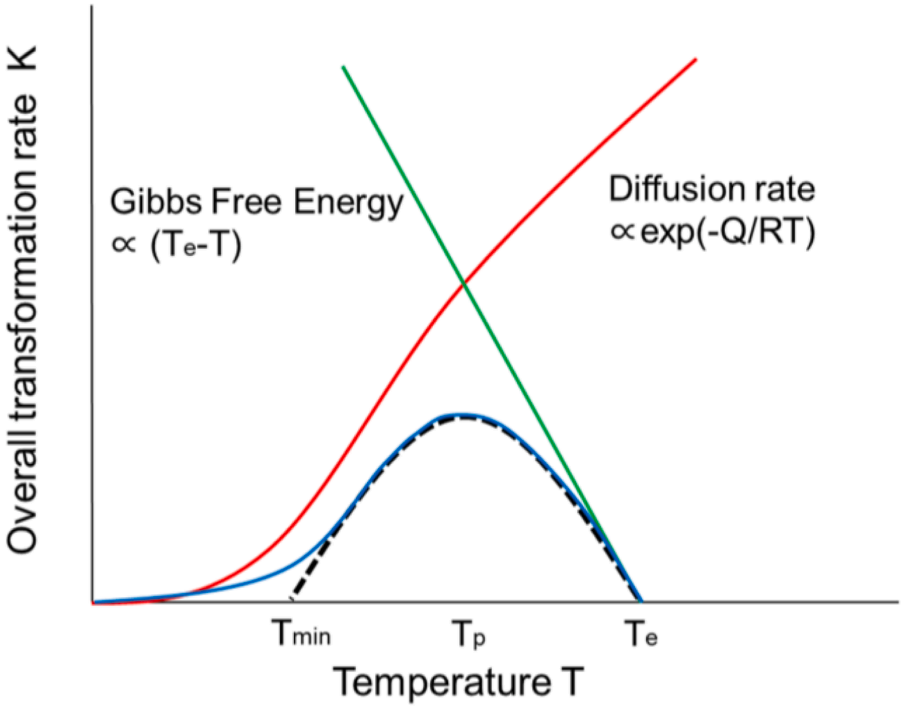

Fig. 5. The schematic diagram of precipitate growth controlled by the interface reaction, or the diffusion. The overall transformation rate as a function of temperature. The dashed line indicates the approximation for the temperature-dependent overall transformation rate could be used by a parabolic function to simplify the analysis. $T_{\min}$stands for the minimum temperature at which transformation occurs, T_p means the critical temperature for maximum overall transformation rate, and T_e represents the equilibrium transformation temperature for nucleation.

To acquire the reliable prediction of the precipitate size with the increase cooling rate, the McLean's theory is applied to build the connection between the average radius of precipitate and cooling rate (McLean, 1984). This model is widely utilized to calculate the precipitate growth during the heat treatment, and by means of the following equation

$$\begin{cases} r^{\alpha} = kt & \alpha = 3 \\ r^{\alpha} = k^{'}t & \alpha = 2 \end{cases} \tag{1}$$

where r is the average radius of precipitate in nm, and t is the time in s. k is a constant and the growth rate in nm^3/s, and $k^{'}$ is a constant and the growth rate in nm^2/s. In addition, k and $k^{'}$ are also temperature dependent value, which can be expressed as $k(T)$ and $k^{'}(T)$ based on the previous work (McLean, 1984), and T is the temperature. In some complicated heat treatment situations, the diffusion controlled equation cannot precisely describe the precipitate growth, hence the interface controlled equation was developed and applied to the precipitate growth process (Lifshitz and Slyozov, 1961; Wagner, 1961; McLean, 1984; Ardell and Ozolins, 2005). Based on the classical Lifshitz and Slyozov and Wagner (LSW) theory, $\alpha = 2$ stands for the precipitate growth controlled by the interface reaction, and $\alpha = 3$ means the precipitate growth controlled by the diffusion. Both two mechanisms during the precipitate growth are operative, however, it is difficult to identify the dominant mechanism. Hence, we choose the equation that can better fit the experimental data.

The precipitation at the peak temperature T_p corresponds to the maximum overall transformation rate K, which relies on two competitive factors: (1) the thermodynamic driving force for nucleation determined by the degree of undercooling $\Delta T = T_e - T$, where T_e is the equilibrium transformation temperature; (2) the diffusivity of the precipitating elements for the growth of the nucleus following an Arrhenius-type temperature dependence. Hence, $K(T)$ can be expressed as

$$K(T) \propto (T_e - T)\exp\left(-\frac{Q}{RT}\right) \tag{2}$$

where T_e is the equilibrium transformation temperature, Q is the activation energy, and R is the gas constant.

Fig. 5 shows that the maximum of the overall transformation rate takes places at an intermediate critical temperature T_p (Papadaki et al., 2018). A convenient approximation for the temperature dependent overall transformation rate could be used by a parabolic function to simplify the analysis, where the transformation rate reaches a maximum when $T = T_p$. Thus, the overall transformation rate can be written approximately in the form

$$K(T) = 1 - (1 - \tau)^2 = \tau(2 - \tau) \tag{3}$$

where a standardized temperature τ is introduced as $\tau = \frac{T_e - T}{T_e - T_p}$.

Assuming the cooling rate from the solution temperature to be constant

$$\frac{d\tau}{dt} = \frac{c}{\Delta T^*} \Rightarrow \tau = \frac{ct}{\Delta T^*} \tag{4}$$

where $\Delta T^* = T_p - T_e$.

Therefore, the overall transformation rate $K(T)$ can be expressed approximately as (Papadaki et al., 2018)

$$K(T) = \frac{ct}{\Delta T^*}\left(2 - \frac{ct}{\Delta T^*}\right) \tag{5}$$

where c is the cooling rate.

Considering the fact that k(or k') and K depend on the temperature, the combination of the Eqs. (1) and (5) can be derived from a mathematical point of view

$$r^{\alpha} = Kt \Leftrightarrow \dot{r} = \frac{1}{\alpha} K r^{1-\alpha} \tag{6}$$

where K is the rate of the overall transformation relying on temperature, and α is dependent on the precipitate growth controlled by the interface reaction and the precipitate growth controlled by the diffusion. It is noted that Eq. (6) is purely empirical formula in which the units of the quantities do not play any role. Nevertheless, previous studies have shown that good agreement with the experiment can be obtained (Papadaki et al., 2018).

By considering Eq. (5), and then separating variables and integrating Eq. (6), we can obtain

$$\int_0^r r^{\alpha-1} dr = \int_0^{t_{\max}} \frac{1}{\alpha} \frac{ct}{\Delta T^*}\left(2 - \frac{ct}{\Delta T^*}\right) dt \tag{7}$$

where $ct/\Delta T^* = 2$ stands for precipitate growth terminates at $\mathrm{t_{max}}$. Thus, based on Eq. (7), the mean particle radius can be written as

$$\frac{r^{\alpha}}{\alpha} = \frac{4}{3\alpha c} \Rightarrow r \propto c^{-1/\alpha} \tag{8}$$

By taking the logarithm on Eq. (8), the precipitate radius and cooling rate obey a linear relationship on a double-logarithmic axis, which is described below

$$\log r = -\frac{1}{\alpha} \log c + B \tag{9}$$

where B is a constant related to the solution heat treatment temperature and alloy composition.

3.2. Model of precipitate volume fraction

The qualitative connection between the volume fraction and cooling rate has been established in a large number of studies (Huang et al., 2018; Semiatin et al., 2018), but the quantitative relationship is still lacking. In the present work, by developing the relationship between the number density of precipitates and the cooling rate, the volume fraction of the precipitates can be predicted in a wide range of cooling rates.

Based on the result of our experiment, the number density of the precipitates can be calculated, and the corresponding function can be expressed as (Semiatin et al., 2015, 2018)

$$N = Ec^F \tag{10}$$

where N is the number density of precipitate, and E and F are the dimensionless constants related to the solution heat treatment temperature and alloy composition. The calculated number density and the cooling rate show a good linear relationship on a double logarithmic axis. In addition, Eq. (10) is purely empirical formula in which the units of the quantities do not play any role.

The radius, number density, and volume fraction of precipitates satisfy the following equation (Cao et al., 2016; Guo et al., 2018; Herrnring et al., 2021)

$$f = \frac{4\pi N r^3}{3} \tag{11}$$

where f is the volume fraction of the precipitate.

Combining Eqs. (8), (10), and (11), the relationship between the volume fraction of precipitate and cooling rate can be given by

$$f = \frac{4A^3 E\pi}{3} c^{F-3/\alpha} \tag{12}$$

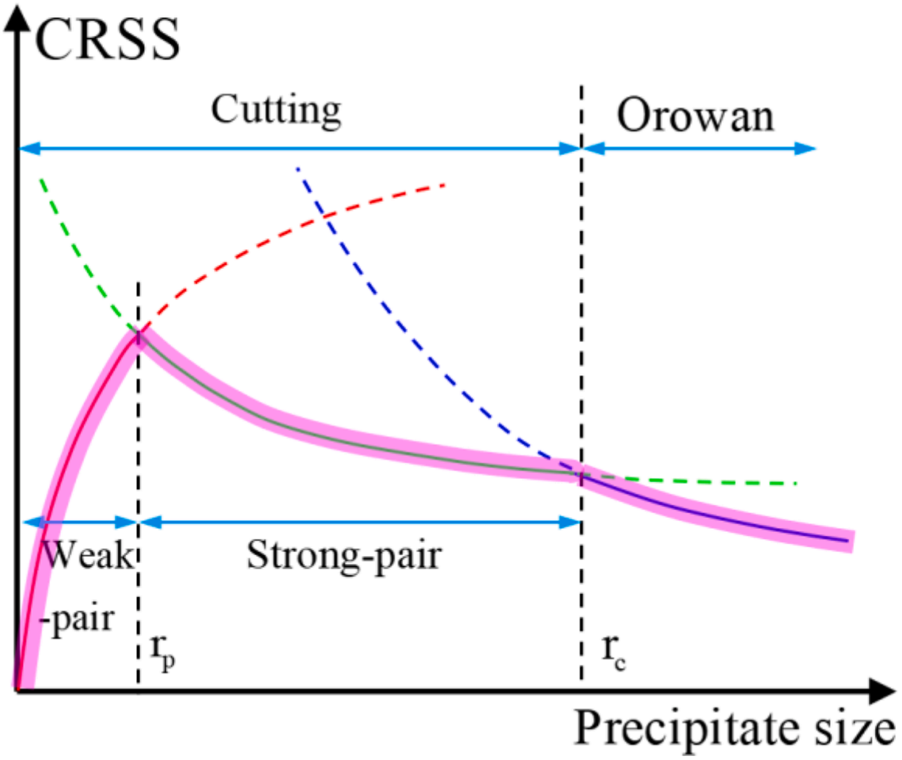

Fig. 6. The CRSS vs. precipitate size. Here, the red line represents the weak-pair coupling mechanism, the green line represents the strong-pair coupling mechanism, and the blue line is the Orowan mechanism. r_p is the critical size for the transformation from the weak-pair to strong-pair coupling, and r_c is the critical size for the transformation from the cutting to the Orowan mechanism. The solid lines denote the effective parts from weak-pair coupling, strong-pair coupling, and Orowan mechanisms. The dash lines denote the ineffective parts (For interpretation of the references to color in this figure legend, the reader is referred to the web version of this article.).

where A denotes $(4/3)^{1/\alpha}$. Subsequently, we can further reasonably predict the yield strength of the alloys using the size and volume fraction of precipitate depending upon the temperature and time. Overall, the cooling rate dependent precipitate size has been deduced based on the previous work. The correlation between the volume fraction of precipitate and cooling rate is for the first time quantitatively established in present work. Although Eq. (12) is empirical formula, it can accurately predict the volume fraction of precipitate with the cooling rate. It would be proved that the latter result is compared with the experiment.

3.3. Precipitate strengthening model

Considering the interaction between the precipitate and dislocation, the precipitate and its composition can be applied, based on the above work. Thus, the critical resolved shear stress (CRSS) is strongly dependent on the precipitate related parameters, including APB energy, precipitate size, and precipitate volume fraction. It has been emphasized that the dislocations travelling in the nickel-based superalloy matrix cannot enter the precipitate without the formation of APB, and therefore that the dislocations must travel through the matrix/precipitate structure in pairs, with a second dislocation removing the APB introduced by the first. The weak-pair coupling means that the spacing of the two paired dislocations is large in comparison with the particle diameter; consequently, the second trailing dislocation is some way behind the first, leaving faulted particles between the two. This situation is applicable to the case of small precipitate. The strong-pair coupling denotes that the spacing of the dislocation pairs becomes comparable to the particle diameter. Thus, any given particle may contain a pair of dislocations, which are now ‘strongly coupled’. This situation is applicable to the case of large precipitate. Based on the comparison between the distance of two paired dislocations and precipitate size, the weak-pair and strong-pair coupling exist.

Here, CRSS of weak-pair coupling is (Reed, 2008; Collins and Stone, 2014; Galindo-Nava et al., 2015; Ghorbanpour et al., 2017; Fang et al., 2019)

$$\tau_{weak} = \frac{\gamma_{APB}}{2b}\left[\left(\frac{6\gamma_{APB}fr}{2\pi T}\right)^{1/2} - f\right] \tag{13}$$

The CRSS of strong-pair coupling can be given by

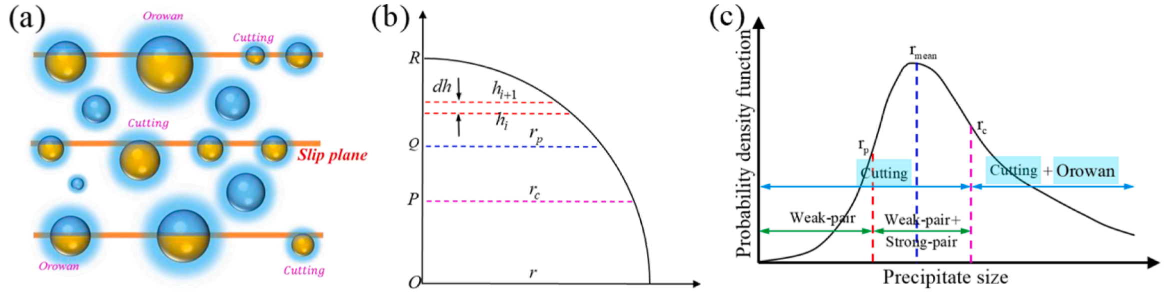

Fig. 7. (a) The illustration of the spatial- and statistical- distribution of the precipitate. (b) The dislocation bypasses through the precipitate in different regions by various mechanisms. The precipitate strengthening in each region is calculated by the numerical integration. h_i and h_{i+1} represent the radii of the i and the $i+1$ parts for the cross-circular area between the slipping plane and precipitate. dh represents the height increment of the infinitesimal. (c) The probability density function vs. precipitate size.

$$\tau_{strong} = \sqrt{\frac{3}{2}}\left(\frac{Gb}{r}\right)\frac{f^{1/2}}{\pi^{3/2}}\left(\frac{2\pi\gamma_{APB}r}{Gb^2}-1\right)^{1/2} \tag{14}$$

where γ_{APB} is the APB energy, b is the magnitude of the Burgers vector, $T = Gb^2/2$ is the line tension of the dislocation, and G is the shear modulus. Especially, the APB energy depends on the composition of the matrix, which is closely related to the cooling rate (Hussein et al., 2017). Here, $7.5 \times 10^{-3}c^{0.697} + 175\ \text{mJ/m}^2$ is used to the current alloys, and its value ranges from 175 to 178.9 mJ/m^2.

When the precipitate size is larger than the critical size for the transformation from cutting to looping mechanism, the CRSS for the dislocation bypassing precipitate through the Orowan mechanism is less than that for the dislocation cutting into precipitates (Ku et al., 2020). Therefore, the Orowan-bypassing mechanism is effective, which can be expressed by

$$\tau_{orowan} = \frac{3Gb}{2L} \tag{15}$$

where L is the mean precipitate spacing, $L = \left(\frac{2\pi}{3f}\right)^{1/2} r$, and the related parameters are listed in Table 4. In addition, the correlations among the weak-pair coupling, strong-pair coupling, and Orowan bypassing mechanisms are illustrated in Fig. 6. Here, the precipitate volume fraction is fixed as a constant in Fig. 6. In Eq. (13), the precipitate strengthening has a positive correlation with the precipitate radius, resulting in the increasing tendency of CRSS for weak-pair coupling with increasing the precipitate radius. In Eqs. (14) and (15), the precipitate strengthening has an inverse correlation with the precipitate radius, resulting in the decreasing tendency of CRSS for strong-pair coupling and Orowan mechanisms with increasing the precipitate radius. Based on the classical theory (see Supplemental Material), the CRSS required for the weak-pair coupling is less than that for the strong-pair coupling and Orowan mechanisms in region $r \le r_p$, thus the weak-pair coupling is the operative mechanism. In region $r_p < r < r_c$, strong-pair coupling is the operative mechanism. In region $r_c \le r$, Orowan mechanism is the operative mechanism. Considering the spatial- and statistical- distribution of the precipitate, we would establish a new precipitate strengthening model based on the classical theory subsequently.

It is significant and necessary to capture the actual precipitate mechanisms for the design of advanced alloys (Iftikhar et al., 2021). In view of the fact that dislocations slip in some certain planes, and precipitates are distributed randomly in the matrix, the relationship of the spatial positions between precipitates and dislocations is considered in the present work (Fig. 7a). Based on the previous experiments (Prikhodko and Ardell, 2003; Goodfellow et al., 2018), some precipitates are cuboidal in form in nickel-based superalloys. Also, this similar phenomenon has been observed by our experiments (see Fig. 3). For the simplification, the classical precipitate strengthening model assume that all precipitates are circular in form (Reed, 2008; Collins and Stone, 2014; Galindo-Nava et al., 2015). Therefore, the cuboidal precipitate would be regarded as a circular shape in Fig. 7a. Here, the strengthening contribution of a large precipitate comes from the three parts, including the weak-cutting region (Eq. (13)), the strong-cutting region (Eq. (14)), and the looping region (Eq. (15)). The dislocation bypasses through the precipitate in the region between '*O*' and '*P*' slip planes by the Orowan mechanism, bypasses through the precipitate in the region between '*P*' and '*Q*' slip planes by the strong-cutting mechanism, and bypasses through the precipitate in the region between '*Q*' and '*R*' slip planes by the weak-cutting mechanism (Fig. 7b). Therefore, for a given precipitate with a size larger than r_c, the effective precipitate strengthening mechanism is the probability-dependent superposition of the weak-pair dislocation mechanism, strong-pair dislocation mechanism, and Orowan mechanism.

In the RQ region, only the weak-pair coupling mechanism is effective. The probability of the dislocation-bypassing RQ region is equal to the ratio between the slip plane R-to-Q distance, l_{RQ}, and the spherical precipitate radius, r (see Fig. 7b). Hence, the probability of this case is

$$p_1 = \frac{l_{RQ}}{r} = 1 - \left(1 - \left(\frac{r_p}{r}\right)^2\right)^{1/2} \tag{16}$$

In the PQ region, there is only the strong-pair coupling mechanism to work. Similarly, the probability in this case is

$$p_2 = \frac{l_{\mathrm{PQ}}}{r} = \left(1-\left(\frac{r_{\mathrm{p}}}{r}\right)^2\right)^{1/2} - \left(1-\left(\frac{r_c}{r}\right)^2\right)^{1/2} \tag{17}$$

In the OP region, there is only the looping mechanism. Similarly, the probability of the dislocation-looping precipitate is

$$p_3 = 1 - p_1 - p_2 \tag{18}$$

To compute the three-parts contributions to the precipitate strengthening, the finite difference method is applied in the interaction between the large precipitate and dislocation. As shown in Fig. 7b, the O-P section, the P-Q section, and the Q-R section can be divided into the n parts, and the CRSS of τ^p_{weak}, τ^p_{strong}, and τ^p_{orowan}, considering the probability effect, can be expressed as

$$\begin{cases} \tau^p_{weak} = \dfrac{1}{n}\displaystyle\sum_{i=1}^{n} \tau_{weak}(h_i), h_i \le r_p \\ \tau^p_{strong} = \dfrac{1}{n}\displaystyle\sum_{j=1}^{n} \tau_{strong}\left(h_j\right), r_p < h_j < r_c \\ \tau^p_{orowan} = \dfrac{1}{n}\displaystyle\sum_{k=1}^{n} \tau_{orowan}(L_k), r_c \le h_k \end{cases} \tag{19}$$

for the τ^p_{weak}, $h_1 = r_w$, and h_{i+1} is equal to $h_{i+1} = \sqrt{r^2 - \left[(r^2-h_i^2)^{1/2} + dh\right]^2}$, where $dh = l_{RQ}/n$ (Fig. 7b). For τ^p_{strong}, $h_1 = r_c$, and h_{j+1} is $h_{j+1} = \sqrt{r^2 - \left[(r^2-h_j^2)^{1/2} + dh\right]^2}$, where $dh = l_{PQ}/n$. For τ^p_{orowan}, $L_k = h_k(2\pi/3f)^{1/2}$, $h_1 = r_c$, and h_{k+1} is $h_{k+1} = \sqrt{r^2 - \left[(r^2-h_k^2)^{1/2} - dh\right]^2}$, where $dh = l_{OP}/n$. Here, dh denotes the space between h_i and h_{i+1}, which is perpendicular to r_p and r_c in Fig. 7b. The parameter "n" in Eq. (19) is an alterable value. The larger the parameter "n", the greater the amount of calculation, but the more accurate the calculation result.

Therefore, for a given precipitate with various sizes, the CRSS, considering the probability-dependent precipitate-bypassing mechanism, can be expressed as

$$\begin{cases} \tau^{new}_{weak} = \tau^p_{weak} & r \le r_p \\ \tau^{new}_{strong} = p_1\tau^p_{weak} + (1-p_1)\tau^p_{strong} & r_p < r < r_c \\ \tau^{new}_{Orowan} = p_1\tau^p_{weak} + p_2\tau^p_{strong} + (1-p_1-p_2)\tau^p_{Orowan} & r_c \le r \end{cases} \tag{20}$$

Subsequently, the statistical distribution of precipitates is considered in the present work. The previous work suggests that the law of the lognormal distribution is used to describe the statistical distribution in the alloys (Collins and Stone, 2014). The region of the precipitate statistical distribution can be divided into three regions, including the weak-pair region, the strong-pair region, and the Orowan looping region (Fig. 7c). Here, in region, $r_p < r \le r_c$, the weak-pair mechanism occurs due to the spatial distribution of precipitates. Similarly, both weak-pair and strong-pair mechanisms are operative in the region, $r > r_c$ (Fig. 7c). The probability density function of the precipitate statistical distribution can be expressed as (Nan and Clarke, 1996)

$$F(r) = \frac{1}{\sqrt{2\pi}\sigma r}\exp\left[-\frac{(\ln(r)-\mu)^2}{2\sigma^2}\right] \tag{21}$$

where μ and σ are the geometric mean value and the geometric standard deviation of ln(r). μ is calculated by Eq. (9). σ is used to describe the distribution of precipitate radii. We firstly measure the precipitate radii and count them as a column chart. Then we fit the column chart to obtain the σ by log-normal probability density function.

In all regions, including $r \le r_p$, $r_p < r \le r_c$, and $r > r_c$, the space-dependent CRSS of τ^s_{weak}, τ^s_{strong}, and τ^s_{orowan} in Fig. 7b can be expressed as

$$\begin{cases} \tau^s_{weak} = \displaystyle\int_0^{r_p} \tau^{new}_{weak}(r)F(r)dr, & r \le r_p \\ \tau^s_{strong} = \displaystyle\int_{r_p}^{r_c} \tau^{new}_{strong}(r)F(r)dr, & r_p < r < r_c \\ \tau^s_{orowan} = \displaystyle\int_{r_c}^{r_{\max}} \tau^{new}_{orowan}(r)F(r)dr, & r_c \le r \end{cases} \tag{22}$$

where τ^s_{weak} is the contribution of all precipitates with sizes less than r_p to contribute to the yielding strength, τ^s_{strong} is the contribution of all precipitates with sizes larger than r_p but less than r_c to contribute to the yielding strength, and τ^s_{orowan} is the contribution of all precipitates with sizes larger than r_c to contribute to the yielding strength. Here, $r_{\max}$ is an artificial value much larger than r_c to avoid

Table 3
The solid solution strengthening parameters, β_i, in a nickel-based alloy.

Element	Co	Cr	Mo	W	Al	Ti	Nb	C	B	Zr	Hf
β_i	10	75	1112	1417	212	1186	1654	1061	-	2359	1401

Table 4
The material parameters used in our model.

Parameters	Symbol	Magnitude
APB energy (mJ/m^2)	γ_{APB}	175–178.9
Magnitude of Burgers vector (nm)	b	0.253
Shear modulus (GPa)	G	67.2
Taylor factor	M	3.06
Hall-Petch constant (MPa/μm)	k_y	750
Constant related to growth mechanism	$1/\alpha_1$	0.481
Constant related to growth mechanism	$1/\alpha_2$	0.119
Constant related to solution temperature	B_1	2.292
Constant related to solution temperature	B_2	1.196
Constant related to alloy composition	E_1	5.37
Constant related to alloy composition	E_2	1303.8
Constant related to alloy composition	F_1	1.09
Constant related to alloy composition	F_2	0.302

errors. τ^{new}_{weak}, τ^{new}_{strong}, and τ^{new}_{Orowan} represent CRSS in three different regions, respectively. *dr* is the differential of *r*.

Compared to the classical precipitate theory where only the mean precipitate size is considered, the present work deals with the precipitate with a single average size as a precipitate group with a log-normal distribution, as shown in Fig. 7c. Here, the total area under the curve is 1 in Fig. 7c. Considering the different operative mechanisms in regions $r \le r_p$, $r_p < r < r_c$, and $r_c \le r$ (Fig. 7c), we compute the precipitate strengthening by three different expressions in Eq. (22) individually. The total contributed strength from the precipitate group is the sum of τ^s_{weak}, τ^s_{strong}, and τ^s_{orowan} in Eq. (22). Hence, considering the spatial- and statistical-distribution of precipitates, the new precipitate strengthening expression of the yielding strength can be written as

$$\sigma_{pre} = M\left(\tau^s_{weak} + \tau^s_{strong} + \tau^s_{orowan}\right) \tag{23}$$

where *M* is the Taylor orientation factor.

3.4. *Yielding strength*

The precipitate parameters are coupled to the precipitate strengthening model, and then the yielding strength in a 3D space can be obtained. The yielding strength includes three strengthening contributions in alloys (Galindo-Nava et al., 2015): (i) grain-boundary strengthening (σ_{GB}); (ii) solid solution strengthening (σ_{ss}); and (iii) precipitate strengthening (σ_{pre}). Therefore, the total yield strength can be given by

$$\sigma_Y = \sigma_{GB} + \sigma_{SS} + \sigma_{pre} \tag{24}$$

The grain-boundary strengthening can be represented by the Hall-Petch relationship (Hall, 1951; Petch, 1953), $\sigma_{GB} = k_Y D^{-1/2}$, where k_Y is a constant (Keller and Hug, 2017), and *D* is the average size of grain. Here, the grain size remains basically unchanged during the aging process. Solid solution strengthening is evaluated by introducing Labusch's theory (Labusch, 1970), and can be given by

$$\sigma_{ss} = (1-f)\left(\sum x_i \beta_i^{3/2}\right)^{2/3} \tag{25}$$

where x_i is the atom fraction of the element, *i*, in the matrix, and β_i is a constant controlled by the local lattice distortion and modulus mismatch of the element, *i*. According to Fleischer's study (Fleischer, 1963), β_i can be derived by $\beta_i = \frac{3}{2}G\left(\eta_i' + 16\delta_i\right)^{3/2}$, where $\eta_i' = |\eta_i| / (\eta_i + 0.5)$ is a constant, $\eta_i = (G_i - G_{Ni})/G_{Ni}$, and $\delta_i = (r_i - r_{Ni})/r_{Ni}$ are the modulus and lattice strain of the element, *i*, respectively, andG_i and r_i represent the shear modulus and atomic radius of the element, *i*, respectively. Here, the estimation of β_i is shown in the Table 3.

The elemental composition of the matrix is changeable during the heat-treatment stage, and the elemental composition of the matrix after the solution heat treatment can be obtained based on the conservation of the solute mass

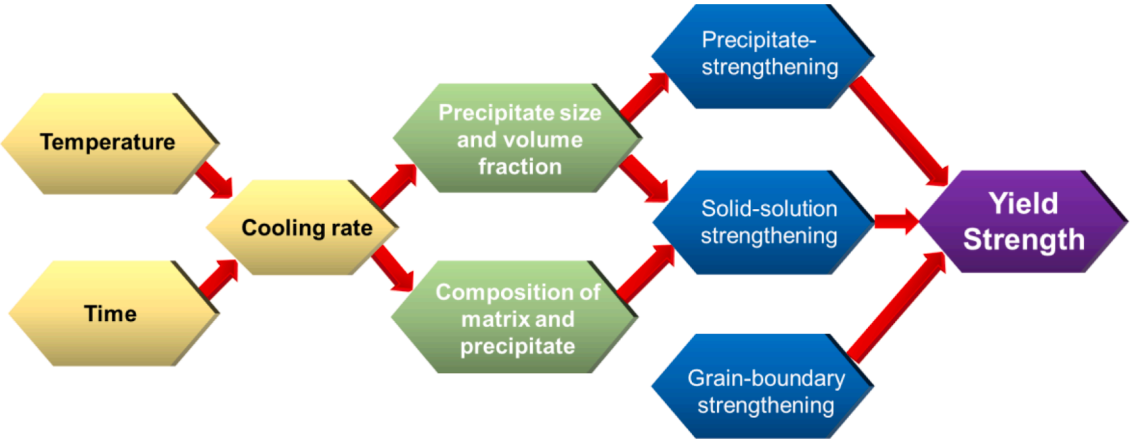

Fig. 8. In a 3D space, the flow chart for predicting the strength, which consists of the strengthening contribution from the cooling rate controlled precipitate, the cooling rate controlled chemical composition of the matrix, and grain boundary.

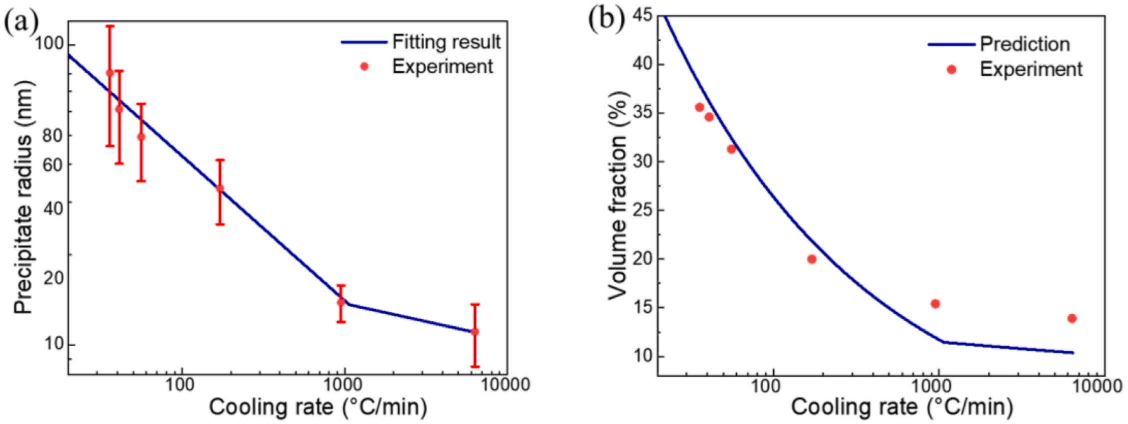

Fig. 9. (a) The precipitate size changes with the increase of the cooling rate, where error bars indicate the precipitate size difference in six different cooling rates. (b) Our prediction of the precipitate volume fraction as a function of cooling rate and its comparison with the experimental result on the log-log plot.

$$x_i = \frac{X_i - f x_{Pi}}{1-f} \tag{26}$$

where X_i is the initial atom fraction of the element, i, and x_{pi} is the atom fraction of the element, i, in the precipitate. The precipitate composition is determined by the equilibrium phase diagram (Table 1).

If Eq. (26) is substituted into Eq. (25), a new solid solution strengthening formula can be obtained

$$\sigma_{ss} = (1-f)^{1/3}\left(\sum \beta_i^{3/2}(X_i - f x_{pi})\right)^{2/3} \tag{27}$$

In the heat treatment process, the precipitates contain a few major elements, such as Co, Al, and Ti. Therefore, the solid solution strengthening is contributed by these several elements.

The parameters $1/\alpha$ and B in Eq. (9) are obtained from the average precipitate radii and cooling rates in Table 2, and the parameters E and F in Eq. (10) are acquired by the average precipitate radii, precipitate volume fractions and cooling rates in Table 2. The experimental data of precipitate size and precipitate volume fraction are used for parameter evaluation. Meanwhile, precipitate volume fraction and Vickers hardness are used for testing our model. The APB energy is estimated, based on a regression type model (Crudden et al., 2014).

Thus, the contribution of precipitate on the yielding strength can be predicted. The flow chart of this work is shown in Fig. 8, which includes identifying the relationship between the precipitate parameter and the cooling rate, the calculation of precipitate strengthening and solid solution strengthening, and the prediction of yielding strength. The details are shown as follows: (i) The precipitate size dependent on the cooling rate is modeled and verified on a double-logarithmic axis; (ii) The correlation between the volume fraction and the cooling rate is obtained by linear regression. (iii) The relationship between the cooling rate and the contributed stress from the

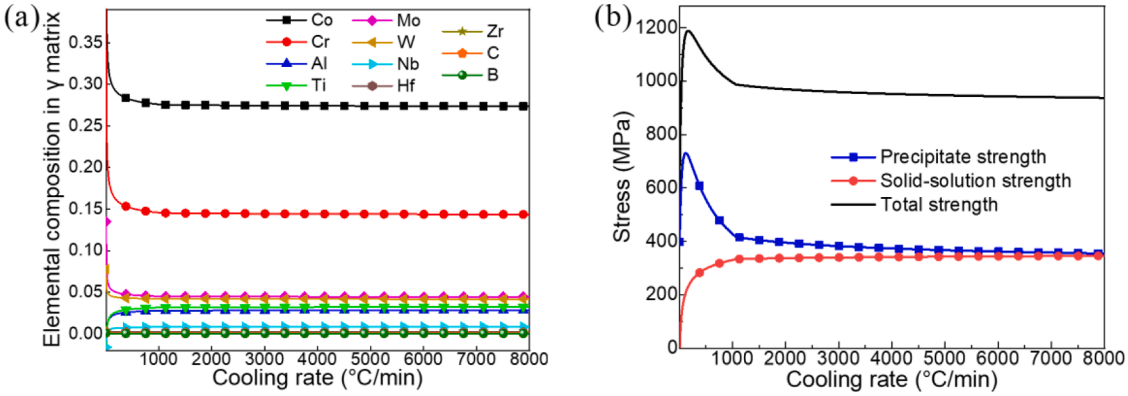

Fig. 10. (a) The elemental compositions in the matrix change with cooling rate. (b) The predictions of solid solution strengthening and precipitate strengthening as a function of cooling rate.

precipitate strengthening and the solid solution strengthening is established. (iv) The total yield strength is a sum of the solid solution strengthening, the precipitate strengthening, and the grain-boundary strengthening.

4. Results and discussion

4.1. Prediction of precipitate size and volume fraction

The microstructure parameters of the precipitate are firstly predicted. In order to identify the reasonability of our model, a comparison of the prediction and our experiment is provided. Fig. 9a shows the relationship between the precipitate size and cooling rate. In order to obtain more accurate prediction, the experimental data of precipitate size has been divided into two groups, namely 0–1000 ℃ and 1000–6346 ℃, to predict the experimental result, which has been reported in the previous work (Mitchell et al., 2008; Chiou et al., 2016). Obviously, the precipitate size from the experimental data is consistent with the calculation from the present work. It indicates that the evolution of the precipitate is dependent on both diffusion and interface reaction. In plenty of previous work (Smith et al., 2018; Wu et al., 2019; Pant et al., 2021), only the diffusion-controlled precipitate growth mechanism is considered, and the parameter, $1/\alpha$, in Eq. (9) is always equal to 0.5. In our model, $1/\alpha$ typically lies between the upper limit of 0.5 and the lower limit of 0.33, which correspond to the interface reaction and diffusion-controlled mechanisms, respectively. If $1/\alpha$ is close to 0.33, the diffusion mechanism is dominant; on the contrary, the interface reaction mechanism is governing. Here, $1/\alpha$ is equal to 0.481, and thus the interface reaction is dominant for the precipitate growth. Furthermore, a comparison between the prediction for the precipitate volume fraction and the experimental data is provided, to verify the validity of the present model (Fig. 9b). As a result, the good agreement is achieved between our prediction and the experimental result.

4.2. Solid solution strengthening vs. precipitate strengthening

To obtain the trend of solid solution strengthening and precipitate strengthening with the cooling rate during the entire solid-solution cooling process in a 3D space (Gao et al., 2020, 2021), the variations of all elemental compositions with increasing the cooling rate in matrix are calculated. According to the previous report (Semiatin et al., 2015), the elemental compositions of precipitates are not obviously affected by the cooling rate during the cooling process. Here, we assume that the precipitate compositions are constant at various cooling rates, which are equal to the compositions of the precipitates in an equilibrium state. The correlation between the cooling rate and the elemental composition in the matrix is shown in Fig. 10a. It is found that the compositions change significantly at a very low cooling rate. The matrix stays in the high-temperature environment for a longer time in the case of low cooling rates, resulting in the higher diffusion rate of various elements (Singh et al., 2013). Moreover, the contents of Co and Cr would strongly affect the yielding strength, compared to the other elements.

The solid solution and precipitate strengthening is calculated in Fig. 10b. Here, the total strength is the sum of the contribution from the precipitate, solid solution, and grain boundary, as mentioned in Eq. (24). The volume fraction of precipitates is negatively correlated with the cooling rate (Li et al., 2021), resulting in more solutes in the matrix at high cooling rate (when the cooling rate is larger than 951 ℃/min). Therefore, the contribution of solid solution strengthening to the yielding strength would gradually increase with the increasing cooling rate. However, the contribution of precipitate strengthening enhances to a maximum value and then decreases slowly. Here, a maximum yield strength at the cooling rate of 166 ℃/min can be predicted. This trend is caused by the complex interaction mechanism between the dislocation and precipitate (Cervellon et al., 2020; Harte et al., 2020). Therefore, the cooperation of the precipitate strengthening and solid solution strengthening causes a maximum yield strength.

In order to further explore the competition and cooperation between solid solution and precipitate strengthening, the contribution of the solid solution and precipitate strengthening is investigated in Fig. 11. The percentage of the contribution from solid solution strengthening to the total strength arises with the increase of cooling rate. The dramatic increase at low cooling rates (when the cooling

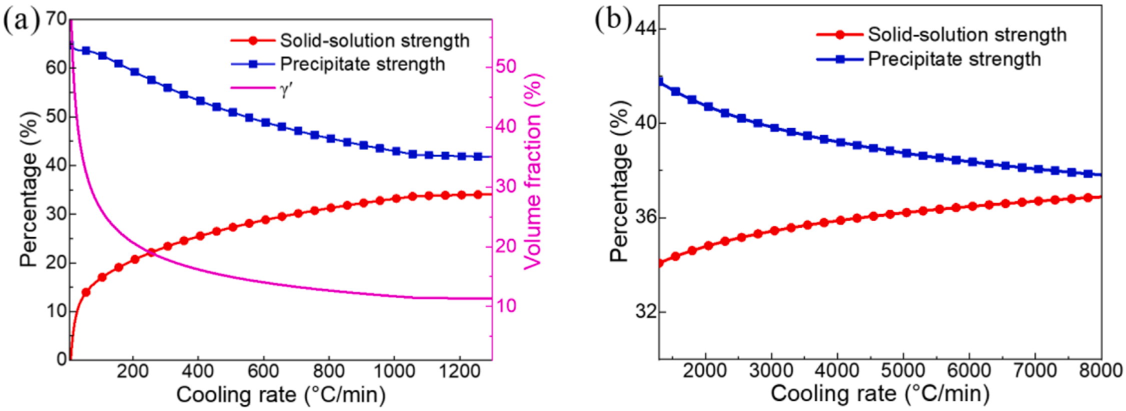

Fig. 11. The competition and cooperation of solid solution and precipitate strengthening during the continuous cooling process.

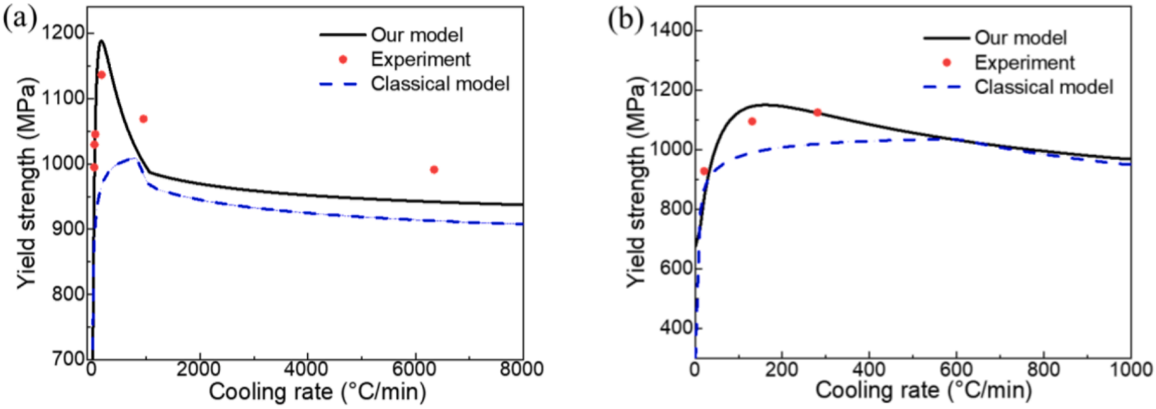

Fig. 12. (a) Our prediction of yield strengths as a function of cooling rate and their comparison with our experimental results. (b) The predicted relationship between the yield strength and cooling rate of another alloy is compared with the corresponding experimental results (Jackson and Reed, 1999).

rate is less than 171 ℃/min) is driven from the suppressed elemental diffusion (Fig. 11). The percentage of the contribution from precipitate strengthening decreases slowly as the cooling rate increases. During the precipitate nucleation stage, a large amount of Co, Cr, Mo, and W diffuse into the precipitates due to their relatively high contents in the matrix (Qu et al., 2020; Zhang et al., 2021), resulting in a very high volume fraction of precipitates and less contribution of solid solution strengthening at a low cooling rate. As the precipitates continue to grow, the elements of Al, Ti, and Nb diffuse from the matrix to the interface; while the elements of Co, Cr, Mo, and W diffuse from the precipitate to the matrix (Chen et al., 2016). This trend leads to the decrease of the precipitate volume fraction and the increase of solid solution strengthening.

4.3. Temperature, time, and composition-dependent yielding strength

The yielding strength of the alloys is studied in a 3D space consisting of the temperature, time, and composition, and their controlling the spatial- and statistical-distribution of the precipitate. Fig. 12 shows the comparison of the yielding strengths between our prediction and experiment in a wide range of cooling rates. Here, the cooling rate contains the temperature and time, and the matrix composition has been determined from our experiment. The maximum yielding strength in our model occurs at the cooling rate of 166 ℃/min. (Fig. 12a). Therefore, the present work can obtain the optimal cooling rate for the maximum strength. In addition, the yield strength calculated agrees well with the existing experimental results (Jackson and Reed, 1999), such as a superalloy U720LI, in the intermediate cooling rates (When the cooling rate is less than 900 ℃/min) (Fig. 12b). Our model can provide the quantitative correlation between the cooling rate and the yield strength.

To verify the reasonability and universality of our developed model, Fig. 13 shows the comparisons of the yield strength obtained from the previous experiments (Mitchell et al., 2008; Tian et al., 2008), the predictions from our model and the classical model for various alloys. The results show that the prediction from our model agrees better with the previous experimental results (Mitchell et al., 2008; Tian et al., 2008), compared with that from the classical model. For all four different alloys, this trend is satisfied, as shown in Fig. 13. Our predicted results show the better agreement not only at the cooling rate less than 200 ℃/min for the large precipitate size,

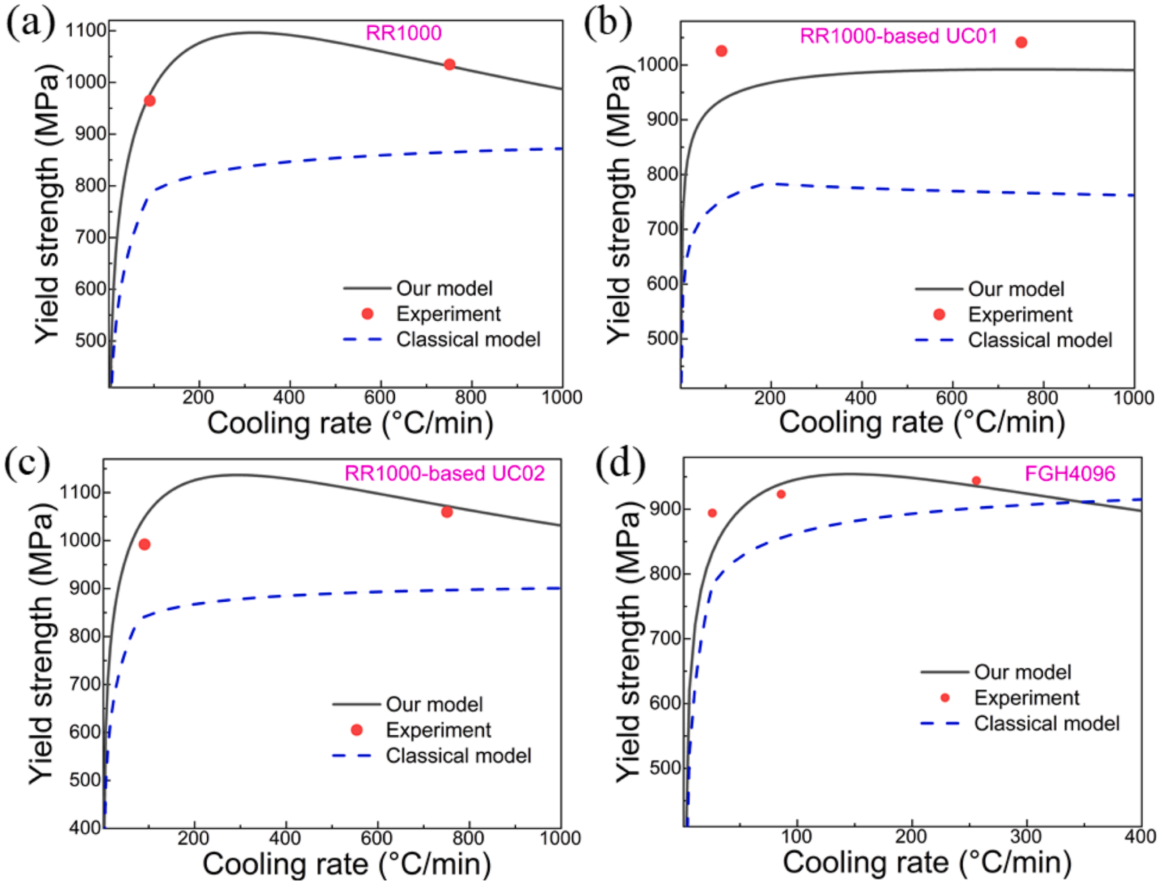

Fig. 13. The correlation between the yield strength and cooling rate is predicted by both our model and classical model, compared with the previous experimental data for RR1000 superalloys (a), RR1000-based UC01 superalloys (b), RR1000-based UC02 superalloys (c), and FGH4096 superalloys (d).

but also at cooling rate larger than 700 ℃/min for the small precipitate size. Compared with the experimental data (Mitchell et al., 2008), the deviations of our model predictions are 1.2, 6.7, and 3.4%, which correspond to the result of RR1000, RR1000-based UC01, and RR1000-based UC02 superalloys. However, the deviations of the classical model predictions are in the range from 15 to 27%. For FGH4096 superalloys (Tian et al., 2008), the deviation of our model prediction is about 3.1%, which is far better than 8.3% of the classical model prediction. Hence, our model is more reasonable to estimate the yield strength after the cooling process in a 3D space.

Therefore, the physical model for predicting the yielding strengths of the alloys in a 3D space are developed. If the alloys can be widely used, they should have the great advantages, such as high strength and good ductility. The ductility is the ability to sustain large deformation, and it is necessary for the precipitate strengthened alloy to provide an early warning of failure. As well known, the deformation of the material depends on the fact, (i) the movement of the defect, such as the dislocation, void, and grain boundary, whose distribution and density are usually uncertain in bulk materials; (ii) the interaction between defects and between defect and precipitate, such as dislocation-void, and dislocation-precipitate; (iii) distribution and concentration of solute elements would affect the defect structure and motion. Thus, a direct connection between atomic scale phenomena and macroscale ductility under loading remains extremely challenging, due to the complex microstructure and interaction. Hence, the quantitative prediction of ductility would be considered in the future, which could provide a framework for the design of alloys with a high strength-yet-toughness.

5. Conclusion

In the present work, we determine the relationship of the cooling rate and the precipitate-related parameters on account of the classic precipitate growth theory, and then propose a microstructure-based physical model to compute the yielding strength in a 3D space. Our novel strength model achieves as high as overall predictable accuracy of 96%, and has filled a long-term gap in the quantitative relationship between heat treatment process and mechanical performance. In order to acquire the better mechanical property, the optimal cooling rate obtained by the present work is 166 ℃/min. Our model reveals the competitive mechanism of the contribution from solid solution strengthening and precipitate strengthening to the yielding strength during the cooling process. The cooling rate would significantly affect the matrix composition and precipitate to control the APB energy. Particularly, the maximal yielding strength depends upon the APB energy, due to the significant contribution of cutting mechanism to the strength. The results not only deeply understand the precipitate evolution and quantitatively predict the precipitate characteristics, but also offer a theoretical guidance for designing the high-property alloys by regulating the heat-treatment process in a 3D space.

CRediT authorship contribution statement

Qihong Fang: Conceptualization, Software, Visualization, Investigation, Data curation, Writing – review & editing, Supervision. **Zhen Huang:** Methodology, Software, Visualization, Investigation, Writing – review & editing. **Li Li:** Methodology, Software, Visualization, Investigation, Writing – review & editing. **Zaiwang Huang:** Investigation, Data curation, Visualization, Supervision, Validation. **Bin Liu:** Methodology, Visualization, Supervision, Validation. **Yong Liu:** Methodology, Visualization, Supervision, Validation. **Jia Li:** Methodology, Software, Data curation, Visualization, Investigation, Writing – review & editing, Supervision. **Peter K. Liaw:** Supervision, Validation.

Declaration of Competing Interest

The authors declare that they have no known competing financial interests or personal relationships that could have appeared to influence the work reported in this paper.

Acknowledgments

The authors would like to deeply appreciate the National Natural Science Foundation of China (12072109, 51871092, and 12172123), and the supports from the National Key Research and Development Program of China (2016YFB0700300). P.K.L. very much appreciates the supports from the National Science Foundation (DMR-1611180 and 1809640) with program directors, Drs. J. Yang, G. Shiflet, and D. Farkas.

Supplementary materials

Supplementary material associated with this article can be found, in the online version, at doi:10.1016/j.ijplas.2021.103152.

References

Ardell, A.J., Ozolins, V., 2005. Trans-interface diffusion-controlled coarsening. Nat. Mater. 4, 309–316.
Atkinson, H.V., Davies, S., 2000. Fundamental aspects of hot isostatic pressing: an overview. Metall. Mater. Trans. A 31, 2981–3000.
Cao, W., Zhang, F., Chen, S.L., Zhang, C., Zhu, J., Semiatin, S.L., Tiley, J.S., 2016. Precipitation modeling of multi-component nickel-based alloys. J. Phase Equilib. Diffus. 37, 491–502.
Cervellon, A., Hémery, S., Kürnsteiner, P., Gault, B., Kontis, P., Cormier, J., 2020. Crack initiation mechanisms during very high cycle fatigue of Ni-based single crystal superalloys at high temperature. Acta Mater. 188, 131–144.
Chen, Y.Q., Francis, E., Robson, J., Preuss, M., Haigh, S.J., 2015. Compositional variations for small-scale gamma prime (γ') precipitates formed at different cooling rates in an advanced Ni-based superalloy. Acta Mater. 85, 199–206.
Chen, Y., Slater, T.J., Bai, M., Mitchell, R., Ciuca, O., Preuss, M., Haigh, S.J., 2016. An investigation of diffusion-mediated cyclic coarsening and reversal coarsening in an advanced Ni-based superalloy. Acta Mater. 110, 295–305.
Chiou, M.S., Jian, S.R., Yeh, A.C., Kuo, C.M., Juang, J.Y., 2016. High temperature creep properties of directionally solidified CM-247LC Ni-based superalloy. Mater. Sci. Eng. A 655, 237–243.
Collins, D.M., Stone, H.J., 2014. A modelling approach to yield strength optimization in a nickel-base superalloy. Int. J. Plast. 54, 96–112.
Crudden, D.J., Mottura, A., Warnken, N., Raeisinia, B., Reed, R.C., 2014. Modelling of the influence of alloy composition on flow stress in high-strength nickel-based superalloys. Acta Mater. 75, 356–370.
Du Plessis, A., Macdonald, E., 2020. Hot isostatic pressing in metal additive manufacturing: X-ray tomography reveals details of pore closure. Addit. Manuf. 34, 101191.
Fang, Q., Li, L., Li, J., Wu, H., Huang, Z., Liu, B., Liaw, P.K., 2019. A statistical theory of probability-dependent precipitation strengthening in metals and alloys. J. Mech. Phys. Solids. 122, 177–189.
Fleischer, R.L., 1963. Substitutional solution hardening. Acta Metall. 11, 203–209.
Francis, E.M., Grant, B.M.B., Da, Fonseca, J.Q., Phillips, P.J., Mills, M.J., Daymond, M.R., Preuss, M., 2014. High-temperature deformation mechanisms in a polycrystalline nickel-base superalloy studied by neutron diffraction and electron microscopy. Acta Mater. 74, 18–29.
Gao, Y.H., Kuang, J., Zhang, J.Y., Liu, G., Sun, J., 2020. Tailoring precipitation strategy to optimize microstructural evolution, aging hardening and creep resistance in an Al–Cu–Sc alloy by isochronal aging. Mater. Sci. Eng. A 795, 139943.
Gao, Y.H., Cao, L.F., Kuang, J., Song, H., Liu, G., Zhang, J.Y., Sun, J., 2021. Solute repositioning to tune the multiple microalloying effects in an Al–Cu alloy with minor Sc, Fe and Si addition. Mater. Sci. Eng. A 803, 140509.
Galindo-Nava, E.I., Connor, L.D., Rae, C.M.F., 2015. On the prediction of the yield stress of unimodal and multimodal γ' nickel-base superalloys. Acta Mater. 98, 377–390.
Ghorbanpour, S., Zecevic, M., Kumar, A., Jahedi, M., Bicknell, J., Jorgensen, L., Knezevic, M., 2017. A crystal plasticity model incorporating the effects of precipitates in superalloys: application to tensile, compressive, and cyclic deformation of Inconel 718. Int. J. Plast. 99, 162–185.
Goodfellow, A.J., Galindo-Nava, E.I., Christofidou, K.A., Jones, N.G., Martin, T., Bagot, P.A.J., Stone, H.J., 2018. Gamma prime precipitate evolution during aging of a model nickel-based superalloy. Metall. Mater. Trans. A 49, 718–728.
Goodfellow, A.J., Galindo-Nava, E.I., Schwalbe, C., Stone, H.J., 2019. The role of composition on the extent of individual strengthening mechanisms in polycrystalline Ni-based superalloys. Mater. Des. 173, 107760.
Guo, H., Enomoto, M., Shang, C.J., 2018. Simulation of bcc-Cu precipitation in ternary Fe-Cu-M alloys. Comput. Mater. Sci. 141, 101–113.

Gupta, S., Bronkhorst, C.A., 2021. Crystal plasticity model for single crystal Ni-based superalloys: capturing orientation and temperature dependence of flow stress. Int. J. Plast. 137, 102896.

Gussev, M.N., Sridharan, N., Thompson, Z., Terrani, K.A., Babu, S.S., 2018. Influence of hot isostatic pressing on the performance of aluminum alloy fabricated by ultrasonic additive manufacturing. Scr. Mater. 145, 33–36.

Hall, E.O., 1951. The deformation and ageing of mild steel: III discussion of results. Proc. Phys. Soc. Lond. B 64, 747–753.

Han, Q., Mertens, R., Montero-Sistiaga, M.L., Yang, S., Setchi, R., Vanmeensel, K., Fan, H., 2018. Laser powder bed fusion of Hastelloy X: effects of hot isostatic pressing and the hot cracking mechanism. Mater. Sci. Eng. A 732, 228–239.

Harte, A., Atkinson, M., Smith, A., Drouven, C., Zaefferer, S., da Fonseca, J.Q., Preuss, M., 2020. The effect of solid solution and gamma prime on the deformation modes in Ni-based superalloys. Acta Mater. 194, 257–275.

Herrnring, J., Sundman, B., Staron, P., Klusemann, B., 2021. Modeling precipitation kinetics for multi-phase and multi-component systems using particle size distributions via a moving grid technique. Acta Mater. 215, 117053.

Herzog, D., Bartsch, K., Bossen, B., 2020. Productivity optimization of laser powder bed fusion by hot isostatic pressing. Addit. Manuf. 36, 101494.

Hirata, T., Kimura, T., Nakamoto, T., 2020. Effects of hot isostatic pressing and internal porosity on the performance of selective laser melted AlSi10Mg alloys. Mater. Sci. Eng. A 772, 138713.

Huang, G., Liu, G.Q., Feng, M., Zhang, M., Hu, B., Wang, H., 2018. The effect of cooling rates from temperatures above the γ' solvus on the microstructure of a new nickel-based powder metallurgy superalloy. J. Alloy. Compd. 747, 1062–1072.

Hussein, A.M., Rao, S.I., Uchic, M.D., Parthasarathy, T.A., El-Awady, J.A., 2017. The strength and dislocation microstructure evolution in superalloy microcrystals. J. Mech. Phys. Solids. 99, 146–162.

Iftikhar, C.M.A., Li, Y.L., Kohar, C.P., Inal, K., Khan, A.S., 2021. Evolution of subsequent yield surfaces with plastic deformation along proportional and non-proportional loading paths on annealed AA6061 alloy: experiments and crystal plasticity finite element modeling. Int. J. Plast. 143, 102956.

Jackson, M.P., Reed, R.C., 1999. Heat treatment of UDIMET 720Li: the effect of microstructure on properties. Mater. Sci. Eng. A 259, 85–97.

Ji, H., Peng, X., Zhang, X., Liu, W., Wu, G., Zhang, L., Ding, W., 2019. Balance of mechanical properties of Mg-8Li-3Al-2Zn-0.5 Y alloy by solution and low-temperature aging treatment. J. Alloy. Compd. 791, 655–664.

Keller, C., Hug, E., 2017. Kocks-mecking analysis of the size effects on the mechanical behavior of nickel polycrystals. Int. J. Plast. 98, 106–122.

Khan, A.S., Meredith, C.S., 2010. Thermo-mechanical response of Al 6061 with and without equal channel angular pressing (ECAP). Int. J. Plast. 26, 189–203.

Ku, A.Y., Khan, A.S., Gnäupel-Herold, T., 2020. Quasi-static and dynamic response, and texture evolution of two overaged Al 7056 alloy plates in T761 and T721 tempers: experiments and modeling. Int. J. Plast. 130, 102679.

Labusch, R., 1970. A statistical theory of solid solution hardening. Phys. Status Solidi. 41, 659–669.

Lifshitz, I.M., Slyozov, V.V., 1961. The kinetics of precipitation from supersaturated solid solutions. J. Phys. Chem. Solid. 19, 35–50.

Li, H.Y., Sun, J.F., Hardy, M.C., Evans, H.E., Williams, S.J., Doel, T.J.A., Bowen, P., 2015. Effects of microstructure on high temperature dwell fatigue crack growth in a coarse grain PM nickel based superalloy. Acta Mater. 90, 355–369.

Li, J., Ding, R., Guo, Q., Li, C., Liu, Y., Wang, Z., Liu, C., 2021. Effect of solution cooling rate on microstructure evolution and mechanical properties of Ni-based superalloy ATI 718Plus. Mater. Sci. Eng. A 812, 141113.

Li, M., Coakley, J., Isheim, D., Tian, G., Shollock, B., 2018. Influence of the initial cooling rate from γ' supersolvus temperatures on microstructure and phase compositions in a nickel superalloy. J. Alloy. Compd. 732, 765–776.

Li, W., Ma, J., Kou, H., Shao, J., Zhang, X., Deng, Y., Fang, D., 2019. Modeling the effect of temperature on the yield strength of precipitation strengthening Ni-base superalloys. Int. J. Plast. 116, 143–158.

Mao, J., Chang, K.M., Yang, W., Ray, K., Vaze, S.P., Ferrer, D.U., 2001. Cooling precipitation and strengthening study in powder metallurgy superalloy U720LI. Metall. Mater. Trans. A 32, 2441–2452.

Mao, J., Chang, K.M., Yang, W., Furrer, D.U., Ray, K., Vaze, S.P., 2002. Cooling precipitation and strengthening study in powder metallurgy superalloy Rene88DT. Mater. Sci. Eng. A 332, 318–329.

Mallikarjuna, H.T., Caley, W.F., Richards, N.L., 2019. The effect of cooling rate on the γ' composition, morphology and corrosion behaviour of IN738LC. Corros. Sci. 149, 37–44.

Masoumi, F., Jahazi, M., Shahriari, D., Cormier, J., 2016. Coarsening and dissolution of γ' precipitates during solution treatment of AD730™ Ni-based superalloy: mechanisms and kinetics models. J. Alloy. Compd. 658, 981–995.

McLean, D., 1984. Predicting growth of γ' in nickel alloys. Metal. Sci. 18, 249–256.

Mitchell, R.J., Preuss, M., Tin, S., Hardy, M.C., 2008. The influence of cooling rate from temperatures above the γ' solvus on morphology, mismatch and hardness in advanced polycrystalline nickel-base superalloys. Mater. Sci. Eng. A 473, 158–165.

Murray, S.P., Pusch, K.M., Polonsky, A.T., Torbet, C.J., Seward, G.G., Zhou, N., Pollock, T.M., 2020. A defect-resistant Co-Ni superalloy for 3D printing. Nat. Commun. 11, 4975.

Nan, C.W., Clarke, D.R., 1996. The influence of particle size and particle fracture on the elastic/plastic deformation of metal matrix composites. Acta Mater. 44, 3801–3811.

Osada, T., Gu, Y., Nagashima, N., Yuan, Y., Yokokawa, T., Harada, H., 2013. Optimum microstructure combination for maximizing tensile strength in a polycrystalline superalloy with a two-phase structure. Acta Mater. 61, 1820–1829.

Papadaki, C., Li, W., Korsunsky, A.M., 2018. On the dependence of γ0 precipitate size in a nickel-based superalloy on the cooling rate from super-solvus temperature heat treatment. Mater 11, 1528.

Pant, N., Verma, N., Ashkenazy, Y., Bellon, P., Averback, R.S., 2021. Phase evolution in two-phase alloys during severe plastic deformation. Acta Mater. 210, 116826.

Panwisawas, C., Tang, Y.T., Reed, R.C., 2020. Metal 3D printing as a disruptive technology for superalloys. Nat. Commun. 11, 2327.

Petch, N.J., 1953. The cleavage strength of polycrystals. J. Iron Steel Inst. 174, 25–28.

Pollock, T.M., 2016. Alloy design for aircraft engines. Nat. Mater. 15, 809–815.

Prikhodko, S.V., Ardell, A.J., 2003. Coarsening of γ' in Ni-Al alloys aged under uniaxial compression: III. Characterization of the morphology. Acta Mater. 51, 5021–5036.

Qin, Z., Wang, Z., Wang, Y., Zhang, L., Li, W., Liu, J., Liu, Y., 2021. Phase prediction of Ni-base superalloys via high-throughput experiments and machine learning. Mater. Res. Lett. 9, 32–40.

Qu, P., Yang, W., Qin, J., Liu, C., Cao, K., Zhang, J., Liu, L., 2020. Precipitation behavior and chemical composition of secondary γ' precipitates in a Re-containing Ni-based single crystal superalloy. Intermetallics 119, 106725.

Radis, R., Schaffer, M., Albu, M., Kothleitner, G., Pölt, P., Kozeschnik, E., 2009. Multimodal size distributions of γ' precipitates during continuous cooling of UDIMET 720 Li. Acta Mater. 57, 5739–5747.

Reed, R.C., 2008. The superalloys: fundamentals and applications. Cambridge University Press.

Reinhart, G., Grange, D., Abou-Khalil, L., Mangelinck-Noël, N., Niane, N.T., Maguin, V., Nguyen-Thi, H., 2020. Impact of solute flow during directional solidification of a Ni-based alloy: *in-situ* and real-time X-radiography. Acta Mater. 194, 68–79.

Rupert, T.J., Trenkle, J.C., Schuh, C.A., 2011. Enhanced solid solution effects on the strength of nanocrystalline alloys. Acta Mater. 59, 1619–1631.

Schleifer, F., Holzinger, M., Lin, Y.Y., Glatzel, U., Fleck, M., 2020. Phase-field modeling of γ/γ'' microstructure formation in Ni-based superalloys with high γ'' volume fraction. Intermetallics 120, 106745.

Semiatin, S.L., Kim, S.L., Zhang, F., Tiley, J.S., 2015. An investigation of high-temperature precipitation in powder-metallurgy, gamma/gamma-prime nickel-base superalloys. Metall. Mater. Trans. A 46, 1715–1730.

Semiatin, S.L., Mahaffey, D.W., Levkulich, N.C., Senkov, O.N., Tiley, J.S., 2018. The effect of cooling rate on high-temperature precipitation in a powder-metallurgy, gamma/gamma-prime nickel-base superalloy. Metall. Mater. Trans. A 49, 6265–6276.

Singh, A.R.P., Nag, S., Chattopadhyay, S., Ren, Y., Tiley, J., Viswanathan, G.B., Banerjee, R., 2013. Mechanisms related to different generations of γ′ precipitation during continuous cooling of a nickel base superalloy. Acta Mater. 61, 280–293.

Singh, S., Hanning, F., Andersson, J., 2020. Influence of hot isostatic pressing on the hot ductility of cast alloy 718: the effect of niobium and minor elements on the liquation mechanism. Metall. Mater. Trans. A 51, 6248–6257.

Smith, T.M., Bonacuse, P., Sosa, J., Kulis, M., Evans, L., 2018. A quantifiable and automated volume fraction characterization technique for secondary and tertiary γ′ precipitates in Ni-based superalloys. Mater. Charact. 140, 86–94.

Sreenu, B., Sarkar, R., Kumar, S.S., Chatterjee, S., Rao, G.A., 2020. Microstructure and mechanical behaviour of an advanced powder metallurgy nickel base superalloy processed through hot isostatic pressing route for aerospace applications. Mater. Sci. Eng. A 797, 140254.

Tian, G., Jia, C., Wen, Y., Liu, G., Hu, B.C., 2008. Cooling γ′ precipitation behavior and strengthening in powder metallurgy superalloy FGH4096. Rare Met. 27, 410–417.

Toda-Caraballo, I., Rivera-Díaz-del-Castillo, P.E., 2015. Modelling solid solution hardening in high entropy alloys. Acta Mater. 85, 14–23.

Wagner, C., 1961. Theorie der alterung von niederschlägen durch umlösen (Ostwald-reifung). Z. Elektrochem. 65, 581–591.

Wang, M.X., Zhu, H., Yang, G.J., Liu, K., Li, J.F., Kong, L.T., 2021. Solid-solution strengthening effects in binary Ni-based alloys evaluated by high-throughput calculations. Mater. Des. 198, 109359.

Wei, B., Wu, W., Xie, D., Nastasi, M., Wang, J., 2021. Strength, plasticity, thermal stability and strain rate sensitivity of nanograined nickel with amorphous ceramic grain boundaries. Acta Mater. 212, 116918.

Wei, Q.S., Xue, P.J., Liu, G.C., Lu, H., Huang, J., Shi, Y.S., 2014. Simulation and verification of near-net shaping a complex-shaped turbine disc by hot isostatic pressing process. Int. J. Adv. Manuf. Technol. 74, 1667–1677.

Wu, H., Huang, Z., Zhou, N., Chen, J., Zhou, P., Jiang, L., 2019. A study of solution cooling rate on γ′ precipitate and hardness of a polycrystalline Ni-based superalloy using a high-throughput methodology. Mater. Sci. Eng. A 739, 473.

Wu, L., Osada, T., Watanabe, I., Yokokawa, T., Kobayashi, T., Kawagishi, K., 2021. Strength prediction of Ni-base disc superalloys: modified γ′ hardening models applicable to commercial alloys. Mater. Sci. Eng. A 799, 140103.

Wu, X., Makineni, S.K., Liebscher, C.H., Dehm, G., Mianroodi, J.R., Shanthraj, P., Gault, B., 2020. Unveiling the Re effect in Ni-based single crystal superalloys. Nat. Commun. 11, 389.

Xu, S., Xiong, L., Chen, Y., McDowell, D.L., 2017. Shear stress-and line length-dependent screw dislocation cross-slip in FCC Ni. Acta Mater. 122, 412–419.

Zhang, J., Huang, T., Lu, F., Cao, K., Wang, D., Zhang, J., Liu, L., 2021. Unveiling the Re segregation at γ/γ′ interface in Ni-based superalloy. Scr. Mater. 204, 114131.